LETTER

https://doi.org/10.1038/s41586-018-0397-3

Cryo–STEM mapping of solid–liquid interfaces and dendrites in lithium–metal batteries

Michael J. Zachman[1], Zhengyuan Tu[2], Snehashis Choudhury[3], Lynden A. Archer[2,3] & Lena F. Kourkoutis[1,4]*

Solid–liquid interfaces are important in a range of chemical, physical and biological processes[1–4], but are often not fully understood owing to the lack of high-resolution characterization methods that are compatible with both solid and liquid components[5]. For example, the related processes of dendritic deposition of lithium metal and the formation of solid–electrolyte interphase layers[6,7] are known to be key determinants of battery safety and performance in high-energy-density lithium-metal batteries. But exactly what is involved in these two processes, which occur at a solid–liquid interface, has long been debated[8–11] because of the challenges of observing such interfaces directly. Here we adapt a technique that has enabled cryo-transmission electron microscopy (cryo-TEM) of hydrated specimens in biology—immobilization of liquids by rapid freezing, that is, vitrification[12]. By vitrifying the liquid electrolyte we preserve it and the structures at solid–liquid interfaces in lithium-metal batteries in their native state, and thus enable structural and chemical mapping of these interfaces by cryo-scanning transmission electron microscopy (cryo-STEM). We identify two dendrite types coexisting on the lithium anode, each with distinct structure and composition. One family of dendrites has an extended solid–electrolyte interphase layer, whereas the other unexpectedly consists of lithium hydride instead of lithium metal and may contribute disproportionately to loss of battery capacity. The insights into the formation of lithium dendrites that our work provides demonstrate the potential of cryogenic electron microscopy for probing nanoscale processes at intact solid–liquid interfaces in functional devices such as rechargeable batteries.

Accurate high-resolution characterization of electrode–electrolyte interfaces is challenging owing to the volatility of commonly used liquid electrolytes, the high chemical reactivity of metal anodes such as lithium and the fact that the region of interest is an interface between two condensed phases of matter. To address this, the liquid is typically removed and the electrode of interest washed and dried before being characterized using traditional methods, which alters the structure and chemistry of the solid–liquid interface[13]. Here, we use cryogenic techniques originally designed for preserving hydrated biological specimens[12] coupled with cryo-focused ion beam (cryo-FIB) and analytical cryo-scanning transmission electron microscopy (cryo-STEM) techniques to access the intact structure and chemistry of dendrites and their interphases in lithium-metal batteries down to the nanoscale.

Figure 1a shows a schematic of the symmetric lithium-metal coin cells used for these experiments (for additional details, see Methods). To preserve the electrolyte on the electrode surface, the cells were opened and the electrode immediately plunge-frozen in a cryogen. To explore the morphology of the anode surface rapidly, we used cryo-FIB to mill a series of cross-sections through structures large enough to be localized by raised regions in the frozen electrolyte (Fig. 1b). We imaged each successive cross-section (Fig. 1c, d), revealing two distinct deposit morphologies, which we refer to as type I and type II dendrites. Type I dendrites are roughly 5 μm across with low curvature, whereas type II dendrites are generally hundreds of nanometres thick and tortuous. We did not observe any spatial correlations between dendrite types, nor cases where one dendrite type clearly formed on the other. To gain insight into their three-dimensional (3D) morphology, we reconstructed the 3D structure of the dendrites from the cross-sectional images (Fig. 1e), as has been demonstrated previously for biological samples[14]. The electrode contact areas for the individual structures can thereby be compared directly, revealing that the widths of type II dendrite contact areas are more than an order of magnitude smaller than those of type I dendrites. This suggests that type II dendrites may become disconnected from the electrode more easily during battery cycling and, in combination with their approximately equal numbers (Fig. 1f) and volumes, contribute disproportionately to capacity fade owing to electrochemically disconnected ('dead') lithium.

Although cryo-FIB techniques alone provide valuable morphological information, we used cryo-STEM and electron-energy-loss spectroscopy (EELS) to obtain high-resolution structural and chemical information about the dendrites and their associated solid–electrolyte interphase (SEI) layers. Electron-transparent cross-sectional lamellae were extracted from plunge-frozen anode–electrolyte interfaces using cryo-FIB lift-out[15] (Fig. 2a, b, Extended Data Fig. 1). High-angle annular dark-field (HAADF) cryo-STEM imaging immediately revealed an extended SEI layer on the type I dendrite, approximately 300–500 nm thick, which was not present on the type II dendrite (Fig. 2c, d). The SEI layer on lithium-metal battery anodes is generally thought to be tens of nanometres thick[7]. Our results suggest that a soft, extended portion of the SEI is removed by the typical washing and drying sample-preparation steps. The remaining SEI material observed by these techniques would then be a thin, compact layer. This is important, in part because it means substantially more lithium is irreversibly lost to the SEI layer than previously thought.

Spectroscopic mapping by EELS shows that the extended type I SEI has an increased concentration of oxygen and lithium compared to the electrolyte and contains essentially no fluorine (Fig. 2e). Although no extended type II SEI is present, there is a thin carbon-free, lithium- and oxygen-rich layer on the type II dendrite surface, approximately 20 nm thick (Fig. 2f). Roughly spherical structures up to micrometres in size, containing carbon, oxygen, lithium and an elevated level of fluorine (Fig. 2e), were frequently observed near both dendrite types (shown near the type I dendrite in Fig. 2a, c) but rarely elsewhere in the sample. Individual elemental maps, including nitrogen, are shown in Extended Data Fig. 2.

By analysing the fine structure of the carbon K-edge using multivariate curve resolution, we observe distinct carbon-bonding environments in the electrolyte, SEI and fluorine-rich structure (Fig. 3a, b, Extended Data Fig. 2b). The increased intensity from C=O bonds in carbonates[16] in the SEI, along with the increased oxygen content and reduced concentration of C–H bonds[16], is consistent with evidence that the SEI consists largely of lithium ethylene dicarbonate in ethylene-carbonate-based electrolytes[9,17,18]. In addition, ethylene gas is produced during the formation of lithium ethylene dicarbonate from ethylene carbonate[9,17–19], which may explain the large bubbles observed in the

[1]School of Applied and Engineering Physics, Cornell University, Ithaca, NY, USA. [2]Department of Materials Science and Engineering, Cornell University, Ithaca, NY, USA. [3]Robert Frederick Smith School of Chemical and Biomolecular Engineering, Cornell University, Ithaca, NY, USA. [4]Kavli Institute at Cornell for Nanoscale Science, Cornell University, Ithaca, NY, USA.
*e-mail: lena.f.kourkoutis@cornell.edu

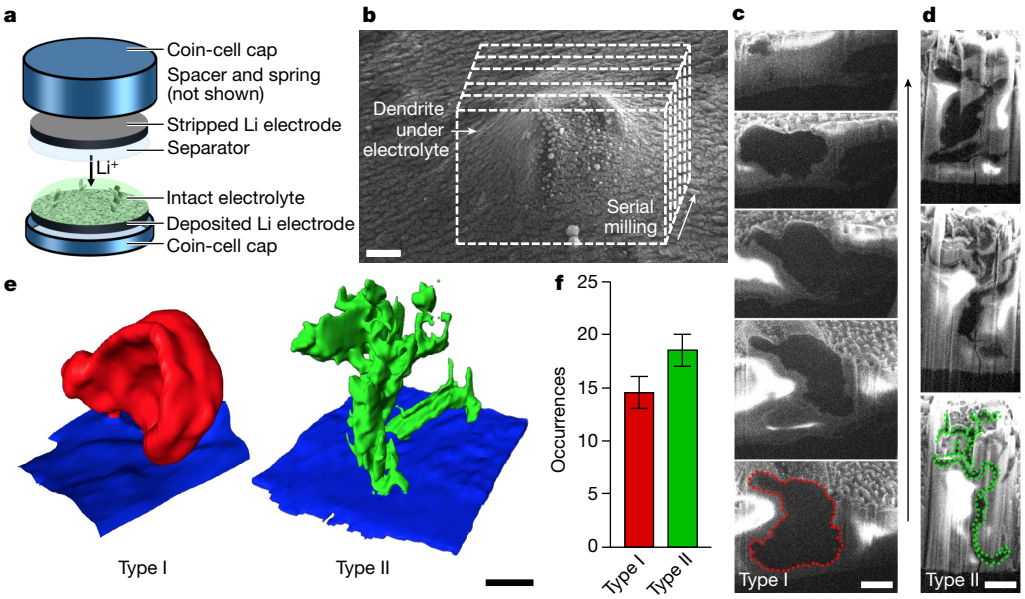

Fig. 1 | Characterization of dendrite morphologies by cryo-FIB. **a**, Coin-cell arrangement used. **b**, Raised regions in the electrolyte frozen on opened coin-cell electrodes reveal buried dendrite locations. The electrolyte surface was sputter-coated with a thin metal layer for increased conductivity. **c**, **d**, Two distinct dendrite morphologies, referred to as type I (**c**) and type II (**d**), were observed in serial cross-sectional images produced by cryo-FIB and cryo-scanning electron microscopy (cryo-SEM). **e**, Three-dimensional reconstructions of the dendrite structures highlight the morphological differences. **f**, Roughly equal numbers of the two morphologies were present across many coin cells. Error bars represent dendrites that were not unambiguously identified. Scale bars, 2 μm (**b**–**d**), 5 μm (**e**).

SEI. The correlation of fluorine and C=C bonds[16] in the fluorine-rich structure may indicate that ethylene is bound to LiF here, the possibility of which has been discussed previously[20]. Although no substantial changes in carbon bonding are observed at the type II dendrite surface (Fig. 3c, d), the fine structure of the oxygen K-edge of the thin type II SEI is consistent with lithium oxide and hydroxide monohydrate (Extended Data Fig. 3a).

EELS of the dendrite interiors show that the type I dendrite contains an appreciable quantity of oxygen, whereas the type II dendrite does not. The two dendrite types are therefore distinct in composition as well as morphology. The fine structures of the lithium and oxygen K-edge (Fig. 4a, b) reveal that the type I dendrite is composed primarily of lithium metal, partially oxidized. The lithium K-edge of the type II dendrite, however, unexpectedly corresponds to pure lithium hydride. Although hydrogen gas is known to be prevalent in cycled lithium batteries[21], only small amounts of LiH have been observed on freshly exposed lithium put in contact with organic electrolytes[22]. However, appreciable quantities have been observed on metal oxide conversion cathodes in lithium-ion batteries[13]. Although LiH is only metastable in electrolytes because it reacts rapidly with trace moisture and solvent molecules to form LiOH and Li_2O[22], these reactions may result in a thin passivating layer on the surface of large LiH structures that preserves the interior material, consistent with the type II dendrite.

Although it might be tempting to assume that the hydrogen required to produce the type II dendrites originates solely from reduction of water impurities in the electrolyte, it was shown recently that the decomposition of electrolyte solvent molecules can produce many times more hydrogen than water impurities provide[19]. By assuming a type II dendrite volume of about 300 μm^3, as determined by our cryo-FIB measurements, a quick calculation reveals that the maximum density of type II dendrites that could form in our cells as a result of hydrogen from water in the electrolyte (less than 10 p.p.m. H_2O) should be roughly an order of magnitude lower than what is actually observed. This suggests that the electrolyte solvent molecules may also be contributing hydrogen. Potential pathways to hydrogen production exist for any hydrogen-containing electrolyte, and therefore all lithium-metal batteries that use traditional organic electrolytes are likely to suffer from LiH dendrite formation and the associated capacity fade. However, the rate of hydrogen production from solvent molecules is a strong function of cell voltage[19], so full cell batteries that use higher-voltage cathodes would produce much larger quantities of hydrogen. This would exacerbate the problem of LiH dendrites in these cells, especially when 5-V-class high-voltage cathode materials that are designed to improve energy density are used.

We additionally examined the plasma resonances of the materials by simultaneously acquired low-loss EELS (Fig. 4c–e). The type I dendrite plasmon suggests that the lithium is only partially oxidized, because appreciably oxidized lithium forms additional resonances at 18 eV and 30 eV[23], which we did not observe. The approximately 13-eV shoulder on the peak corresponding to the type II dendrite also provides further evidence for the presence of LiH, because the hydrogen K-edge is found at 13.6 eV. Using the distinct low-loss spectra of the two dendrite materials, we map their spatial distribution within the dendrites (Fig. 4c, d). This mapping demonstrates that small LiH regions are also present on the surface of the type I dendrite and that a lithium particle is present on the tip of the type II dendrite. These results are summarized in Extended Data Table 1 and Extended Data Fig. 2d.

The lithium particle on the tip and the uniformity of the LiH within the type II dendrites, as well as their aspect ratio, suggest a root or tip growth mode. Grain boundaries have been shown to increase hydrogen diffusion through some metals[24], and hydrogen selectively penetrating into an electrode grain boundary or a lithium-particle–electrode interface could initiate LiH formation. The resulting volume expansion would lift the particle or electrode grain away from the electrode surface, leading to the observed lithium tip on the dendrite (Fig. 4d). Growth would then probably proceed mainly at the dendrite–electrode interface, owing to the poor electrical conductivity of LiH[25]. Although the formation of LiH is reversible[13], the reverse reaction would also occur primarily at the base. Furthermore, LiH is much more brittle than lithium metal[26]. These facts, combined with the low electrode contact area of the type II dendrites, suggest that the type II dendrites become disconnected from the electrode more easily during cycling than do type I dendrites. Because the total volume and number of dendrites are comparable for both types, type II dendrites may, therefore, contribute disproportionately to capacity fade by orphaned or disconnected lithium. The thickness of the type I SEI layer also means that it contributes

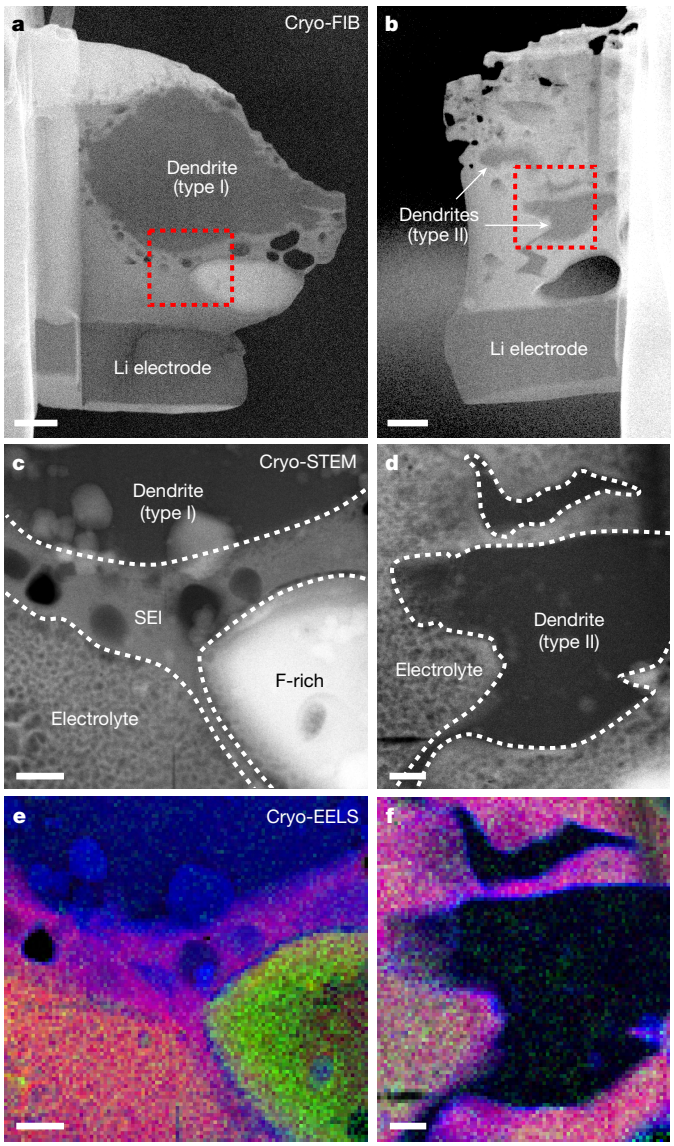

Fig. 2 | Structure and elemental composition of dendrites and their interphase layers in electron-transparent lamellae. a, **b**, Electron-transparent cryo-FIB lift-out lamellae of type I (**a**) and type II (**b**) dendrites. **c**, **d**, HAADF cryo-STEM imaging reveals an extended SEI layer on the type I dendrite (**c**), but not on the type II dendrite (**d**). **e**, **f**, EELS elemental mapping shows that both SEIs are oxygen-rich, but that the type II SEI contains no carbon (contrast has been adjusted for clarity; raw data are shown in Extended Data Fig. 2). The type I dendrite has an appreciable oxygen content (**e**), whereas the type II dendrite does not (**f**). Fluorine-rich structures were often observed near both dendrite types. Scale bars, 1 μm (**a**, **b**), 300 nm (**c**–**f**).

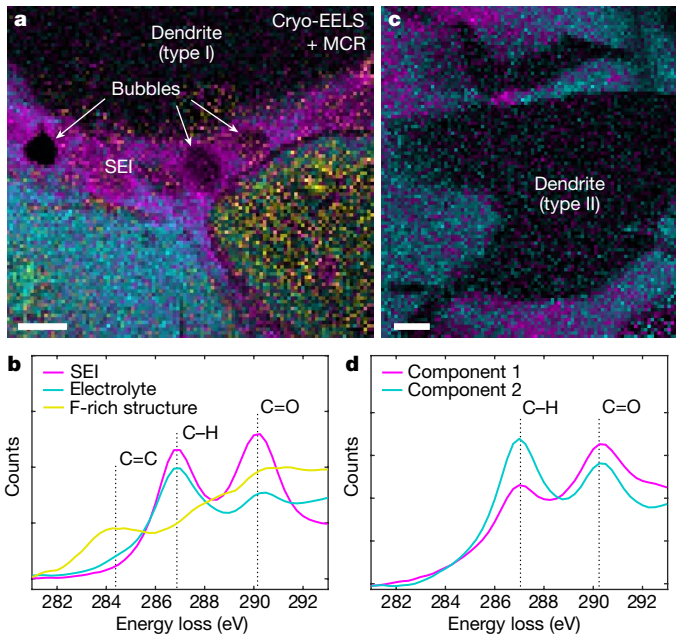

Fig. 3 | Analysis of the carbon-bonding environment near the dendrites. a, Spatial variation of the fine structure of the carbon K-edge near a type I dendrite, obtained from EELS, showing distinct carbon-bonding environments, as determined using multivariate curve resolution (MCR; contrast has been adjusted for clarity; raw data are shown in Extended Data Fig. 2). **b**, The increased carbonate C = O peak is consistent with a lithium ethylene dicarbonate SEI layer. Ethylene gas produced during SEI formation may explain the SEI bubbles seen in **a** and the C = C peak in the fluorine-rich structure. **c**, **d**, Two carbon components were present in the electrolyte around the type II dendrite, but were not localized along the dendrite surface. Scale bars, 300 nm.

more to the loss of lithium material than previously thought; we estimate, however, that an order of magnitude more lithium is contained within the type II dendrites than in the type I SEI layers. Minimizing the formation of LiH dendrites is therefore critical to improving the longevity of lithium-metal batteries.

Our results suggest that preventing the formation of type II dendrites may hinge on a careful choice of solvents and salts to eliminate hydrogen-containing species in the electrolyte and to form interphase layers that are better able to protect the anode. One way to achieve these goals would be to replace hydrogen in the solvent molecules with other elements to generate alternative species in the electrolyte. For example, we hypothesize that a properly chosen material would result in a hydrogen-deprived and fluorine-rich environment in which sacrificial, low-stability-window fluorinated components preferentially react at the electrodes relative to carbonate solvents, resulting in fluorine-rich species in the electrolyte. This would both starve the system of hydrogen and promote the formation of a beneficial LiF-rich barrier layer on the surface of the anode[27,28], stunting the growth of LiH dendrites and reducing capacity fade. Although recent studies that used high-concentration full-fluoride electrolytes are consistent with our predictions[29], maintaining the high fluorine-donating salt content of such electrolytes is currently impractical because of the high cost of the salt. There is therefore reason to explore alternative hydrogen-free electrolyte materials that are as effective using different salts at lower concentrations.

As a test of the above hypothesis, we performed cryo-FIB, cryo-STEM EELS and electrochemical experiments on cells prepared with a full-fluoride-type electrolyte using a lower salt concentration of a less expensive salt (2 M $LiPF_6$) than in previous reports; a fully fluorinated solvent, fluoroethylene carbonate, was used in these electrolyte compositions. The results are shown in Extended Data Fig. 4. Consistent with our hypothesis, we found that this fluorinated electrolyte suppresses the formation of LiH dendrites substantially and greatly alters the lithium deposition. Localized structures are still present, but rather than type I dendrites the deposits are much larger, with an inner structure consisting of many smaller 'blocks' separated by SEI layers. These blocks are composed of partially oxidized lithium, as with the type I dendrites, which was confirmed by cryo-STEM EELS of structures prepared by cryo-FIB lift-out. The electrochemical performance was correspondingly enhanced, with higher Coulombic efficiency and greatly reduced capacity fade, as shown in a lithium versus stainless steel set-up and in a full-cell battery that used a nickel manganese cobalt oxide cathode. Although this demonstrates the feasibility of dendrite suppression and improved battery performance by introducing fluorinated electrolytes, the concepts outlined above could potentially be further developed by integrating the alternative electrolyte species into cross-linkable structures, such as those reported recently[30]. This would result in a

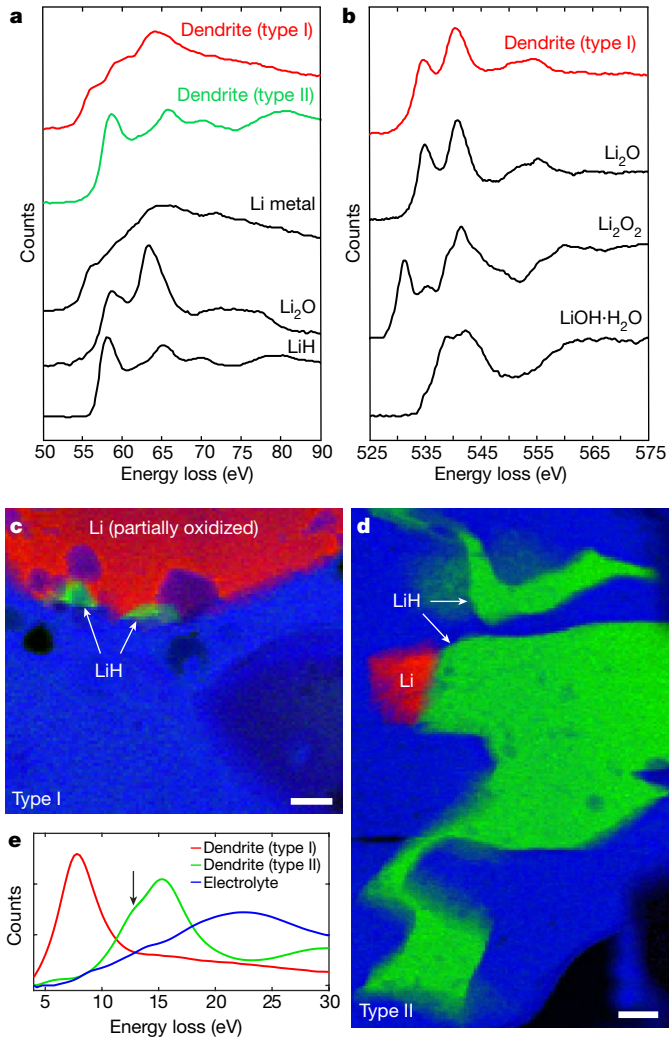

Fig. 4 | Determination and mapping of dendrite composition. **a**, **b**, Comparison of the fine structures of the lithium (**a**) and oxygen (**b**) K-edge of the dendrites (coloured lines) with reference materials (black) reveals that the type I dendrite was partially oxidized lithium metal, whereas the type II dendrite was uniform lithium hydride. **c**–**e**, Mapping of the lithium metal and hydride low-loss EELS spectra (**e**) reveals that the type I dendrite was only slightly oxidized and had small LiH regions at its surface (**c**), whereas the type II dendrite had a lithium particle tip (**d**) (contrast has been adjusted for clarity; raw data are shown in Extended Data Fig. 2). The arrow in **e** denotes the hydrogen K-edge that appears at about 13 eV in LiH. Scale bars, 300 nm.

hydrogen-deprived and halide-rich electrolyte environment that simultaneously form lithium-halide-rich and elastic interphases that are able to flex to accommodate changes in the volume of the lithium anode, thus providing further protection against both LiH and traditional lithium-metal dendrites. Cryo-FIB and analytical cryo-STEM techniques have thus provided us access to the nanoscale structure and composition of intact solid–electrolyte interfaces in lithium-metal batteries, revealing the existence of LiH dendrites and extended SEI layers on lithium metal dendrites, and allowed us to propose pathways to overcoming their detrimental effects.

Online content

Any Methods, including any statements of data availability and Nature Research reporting summaries, along with any additional references and Source Data files, are available in the online version of the paper at https://doi.org/10.1038/s41586-018-0397-3.

Received: 17 January 2018; Accepted: 4 July 2018;
Published online 15 August 2018.

1. Wu, Y. & Yang, P. Direct observation of vapor–liquid–solid nanowire growth. *J. Am. Chem. Soc.* **123**, 3165–3166 (2001).
2. Weiner, S. & Addadi, L. Crystallization pathways in biomineralization. *Annu. Rev. Mater. Res.* **41**, 21–40 (2011).
3. Stamenkovic, V. R., Strmcnik, D., Lopes, P. P. & Markovic, N. M. Energy and fuels from electrochemical interfaces. *Nat. Mater.* **16**, 57–69 (2017).
4. Tarascon, J.-M. & Armand, M. Issues and challenges facing rechargeable lithium batteries. *Nature* **414**, 359–367 (2001).
5. Zaera, F. Probing liquid/solid interfaces at the molecular level. *Chem. Rev.* **112**, 2920–2986 (2012).
6. Tikekar, M. D., Choudhury, S., Tu, Z. & Archer, L. A. Design principles for electrolytes and interfaces for stable lithium-metal batteries. *Nat. Energy* **1**, 16114 (2016).
7. Cheng, X.-B. et al. A review of solid electrolyte interphases on lithium metal anode. *Adv. Sci.* **3**, 1500213 (2016).
8. Yamaki, J. et al. A consideration of the morphology of electrochemically deposited lithium in an organic electrolyte. *J. Power Sources* **74**, 219–227 (1998).
9. Aurbach, D. Review of selected electrode-solution interactions which determine the performance of Li and Li ion batteries. *J. Power Sources* **89**, 206–218 (2000).
10. Bai, P., Li, J., Brushett, F. R. & Bazant, M. Z. Transition of lithium growth mechanisms in liquid electrolytes. *Energy Environ. Sci.* **9**, 3221–3229 (2016).
11. Kushima, A. et al. Liquid cell transmission electron microscopy observation of lithium metal growth/dissolution: root growth, dead lithium and lithium flotsams. *Nano Energy* **32**, 271–279 (2017).
12. Dubochet, J. et al. Cryo-electron microscopy of vitrified specimens. *Q. Rev. Biophys.* **21**, 129–228 (1988).
13. Hu, Y.-Y. et al. Origin of additional capacities in metal oxide lithium-ion battery electrodes. *Nat. Mater.* **12**, 1130–1136 (2013).
14. Heymann, J. A. W. et al. Site-specific 3D imaging of cells and tissues with a dual beam microscope. *J. Struct. Biol.* **155**, 63–73 (2006).
15. Zachman, M. J., Asenath-Smith, E., Estroff, L. A. & Kourkoutis, L. F. Site-specific preparation of intact solid–liquid interfaces by label-free in situ localization and cryo-focused ion beam lift-out. *Microsc. Microanal.* **22**, 1338–1349 (2016).
16. Cody, G. D. et al. Quantitative organic and light-element analysis of comet 81P/Wild 2 particles using C-, N-, and O-mu-XANES. *Meteorit. Planet. Sci.* **43**, 353–365 (2008).
17. Yang, C. R., Wang, Y. Y. & Wan, C. C. Composition analysis of the passive film on the carbon electrode of a lithium-ion battery with an EC-based electrolyte. *J. Power Sources* **72**, 66–70 (1998).
18. Zhuang, G. V., Xu, K., Yang, H., Jow, T. R. & Ross, P. N. Lithium ethylene dicarbonate identified as the primary product of chemical and electrochemical reduction of EC in 1.2 M LiPF 6/EC:EMC electrolyte. *J. Phys. Chem. B* **109**, 17567–17573 (2005).
19. Metzger, M., Strehle, B., Solchenbach, S. & Gasteiger, H. A. Origin of H_2 evolution in LIBs: H_2O reduction vs. electrolyte oxidation. *J. Electrochem. Soc.* **163**, A798–A809 (2016).
20. Szczęśniak, M. M. & Ratajczak, H. Ab initio calculations on the lithium fluoride–ethylene complex. *J. Chem. Phys.* **67**, 5400–5401 (1977).
21. Onuki, M. et al. Identification of the source of evolved gas in Li-ion batteries using $^{\#2}$#1 -labeled solvents. *J. Electrochem. Soc.* **155**, A794–A797 (2008).
22. Aurbach, D. & Weissman, I. On the possibility of LiH formation on Li surfaces in wet electrolyte solutions. *Electrochem. Commun.* **1**, 324–331 (1999).
23. Liu, D.-R. & Williams, D. B. The electron-energy-loss spectrum of lithium metal. *Philos. Mag. B* **53**, L123–L128 (1986).
24. Oudriss, A. et al. The diffusion and trapping of hydrogen along the grain boundaries in polycrystalline nickel. *Scr. Mater.* **66**, 37–40 (2012).
25. Islam, A. K. M. A. Lighter alkali hydride and deuteride. *Phys. Status Solidi b* **180**, 9–57 (1993).
26. Settouti, N. & Aourag, H. Structural and mechanical properties of alkali hydrides investigated by the first-principles calculations and principal component analysis. *Solid State Sci.* **58**, 30–36 (2016).
27. Choudhury, S. & Archer, L. A. Lithium fluoride additives for stable cycling of lithium batteries at high current densities. *Adv. Electron. Mater.* **2**, 1500246 (2016).
28. Lu, Y., Tu, Z. & Archer, L. A. Stable lithium electrodeposition in salt-reinforced electrolytes. *Nat. Mater.* **13**, 961–969 (2014).
29. Suo, L. et al. Fluorine-donating electrolytes enable highly reversible 5-V-class Li metal batteries. *Proc. Natl Acad. Sci. USA* **115**, 1156–1161 (2018).
30. Zhao, Q. et al. Building organic/inorganic hybrid interphases for fast interfacial transport in rechargeable metal batteries. *Angew. Chem. Int. Ed.* **57**, 992–996 (2018).

Acknowledgements We thank D. Muller, H. Abruña and J. Noble for discussions. M.J.Z. and L.F.K. acknowledge support by the NSF (DMR-1654596) and the Packard Foundation. Z.T., S.C. and L.A.A. acknowledge support from the Department of Energy, Advanced Research Projects Agency - Energy (ARPA-E) through award number DE-AR0000750. This work made use of the Cornell Center for Materials Research (CCMR) Shared Facilities with funding from the NSF MRSEC programme (DMR-1719875). Additional support for the FIB/SEM cryo-stage and transfer system was provided by the Kavli Institute at Cornell and the Energy Materials Center at Cornell, DOE EFRC BES (DE-SC0001086). The FEI Titan Themis 300 was acquired through NSF MRI-1429155, with additional support from Cornell University, the Weill Institute and the Kavli Institute at Cornell. This work made use of electrochemical characterization facilities in the KAUST-CU Center for Energy and Sustainability, supported by

the King Abdullah University of Science and Technology (KAUST) through award number KUS-C1-018-02.

Author contributions M.J.Z. and L.F.K. conceived the project and wrote the manuscript. M.J.Z. prepared samples, performed the experiments and analysed the data. Z.T. constructed, cycled and disassembled the traditional electrolyte coin cell batteries. S.C. constructed, cycled, dissembled and measured the electrochemical properties of the full-fluoride and traditional electrolyte coin cell batteries displayed in Extended Data Figure 4b–f. Z.T. and L.A.A. provided assistance with interpretation of the data and made revisions to the manuscript.

Competing interests The authors declare no competing interests.

Additional information
Extended data is available for this paper at https://doi.org/10.1038/s41586-018-0397-3.
Reprints and permissions information is available at http://www.nature.com/reprints.
Correspondence and requests for materials should be addressed to L.F.K.
Publisher's note: Springer Nature remains neutral with regard to jurisdictional claims in published maps and institutional affiliations.

METHODS

Instrumentation and experimental details. We used an FEI Strata 400S DualBeam focused ion beam/scanning electron microscope system (FIB/SEM) to characterize and prepare samples. It was fitted with a Quorum PP3010T cryo-SEM/FIB system, which included a liquid nitrogen cold stage and an anticontaminator in the main FIB chamber, a preparation chamber (for sputter coating) with a separate cold stage and an anticontaminator attached to the FIB and separated by a valve, a stand-alone workstation for freezing and loading samples onto the specimen shuttle, and a vacuum transfer device for transporting samples between the workstation and preparation chamber. In addition, we installed an Oxford OmniProbe Cryoshaft on our OmniProbe 200 nanomanipulator, which is thermally isolated from the room-temperature shaft by a ceramic section and cooled by a copper braid attached to the anticontaminator[15]. Preparation of lamellae by cryo-FIB lift-out was carried out using techniques described previously[15]. All milling was performed at an ion beam voltage of 30 kV. Trenches to form the initial lamella were generally milled with a beam current of a few nanoamps. Thinning of the lamella was first conducted with a beam current of hundreds of picoamps, decreasing with lamella thickness to a final thinning with tens of picoamps. After cryo-FIB lift-out preparation, cryo-STEM samples were transferred back into liquid N_2 in the workstation where they were loaded into cryogenic sample storage boxes and transferred to a large liquid N_2 storage dewar.

Cryo-STEM characterization of these samples was performed on an aberration-corrected FEI Titan Themis operated at 300 kV. The microscope was equipped with an X-FEG high-brightness gun and a high-resolution Gatan imaging filter (GIF Quantum 965) for EELS. Standard Gatan side-entry cryo-transfer holders (model 626 and model 915) enabled transfer of the samples into the microscope and maintained their temperature near −180 °C throughout the experiment. The samples were loaded into the holder under liquid N_2 to minimize ice contamination. During transfer into the vacuum of the microscope, the sample was enclosed by a cryo-shutter which minimized ice build-up. No EELS edges beyond those discussed in the main text were observed in the dendrites between the Li K-edge at 55 eV and about 730 eV, including nitrogen, which rules out reactions with air or liquid N_2 during specimen preparation and transfer (Extended Data Fig. 5). While throughput of the cryo-FIB lift-out/cryo-STEM workflow is continuing to be improved, it can approach that of room-temperature FIB and STEM techniques with proper optimization. Multiple lamellae were prepared for analysis by cryo-STEM for this project. Additional examples are shown in Extended Data Fig. 1i–k, including an uncycled electrode for reference, and two containing type II dendrites. The O K-edge reference spectra for Li_2O_2 and LiOH and the Li K-edge reference spectrum for LiH were taken on a 200-kV FEI F20 using the same cryo-transfer holders and loading techniques.

The probe current for EELS maps on the Titan was around 25 pA, confirmed by measurement on a direct electron detector with a high dynamic range[31], and pixel dwell times were 10–50 ms. The electron dose applied during acquisition of the spectroscopic maps shown in the main text was 5×10^1–5×10^2 e^- Å^{-2}. The small bubbles in the electrolyte appeared rapidly, beginning by the time the first image was taken, with a total dose below 10 e^- Å^{-2}. These bubbles were probably hydrogen liberated from the electrolyte solvent molecules[32], since C and O K-edge fine structures in carbonates are known to be stable under the beam up to a dose of about 750 e^- Å^{-2} at room temperature under a 200-keV electron beam[33]. The threshold damage for these materials under our cryogenic conditions using a 300-keV beam should be higher than this[32]. A series of maps of the electrode–electrolyte interface taken at various total doses is shown in Extended Data Fig. 6a, c, demonstrating the doses at which different types of damage occur. The damage mechanisms of these carbonate solvents are liberation of hydrogen at low doses, resulting in structural changes such as the bubbling observed. At doses of more than 10^3 e^- Å^{-2}, mass loss becomes important and the fine structure of the approximately 287-eV peak is affected. At 10^4 e^- Å^{-2} the mass loss is severe, producing holes in the sample and leaving behind mainly the carbonate portion of the solvent molecules. However, the fine structure associated with this part of the molecule survives high doses. These findings are summarized in Extended Data Table 2. On the basis of our damage analysis, we do not expect the fine structure to have been altered in the maps shown in the main text, although slight structural modifications were present, as expected (Extended Data Fig. 6d, e).

LiH spectra have been measured previously using various techniques, and are not all in agreement[34–36]. The moisture sensitivity of the material may explain the disagreement. While precautions were taken in previous work to avoid air exposure, such as cleaving the LiH in vacuum[34] or transferring it to the microscope in an argon bag[35], reactions with small amounts of contaminants could still occur at room temperature. Accurate spectra could be obtained either by measuring a bulk sample, as the passivating layer would enable the majority of the material to remain unreacted, or by maintaining the sample at cryogenic temperatures, since reactions with contaminants would be essentially eliminated. As expected, the spectra from samples measured in bulk or at cryogenic temperatures are in agreement with each other[34,36] and with our data. The difficulty of characterizing unaltered LiH may be one reason why LiH dendrites have not been observed before, and is an important example of how cryogenic techniques such as cryo-FIB lift-out and cryo-STEM enable accurate characterization of systems with reactive materials as well as of solid–liquid interfaces.

Acquisition of reference spectra. The reference spectra for the lithium metal and Li_2O samples were acquired on the Titan in similar conditions to those described above. The Li K-edge for lithium metal was recorded on an uncycled lithium electrode and the Li_2O spectrum was recorded on a lithium electrode oxidized in the microscope by warming to room temperature and exposing the electrode to the beam. Both samples were produced by cryo-FIB lift-out. The electron dose for the metal spectrum was 10^4 e^- Å^{-2} and no change in fine structure was recorded by doubling this dose. The oxide spectra were acquired with a total dose of around 10^2 e^- Å^{-2}. While we observed that other lithium–oxygen compounds converted to Li_2O under the beam, no change to the Li_2O fine structure was observed at high doses.

We acquired the lithium peroxide and hydroxide reference materials from Sigma Aldrich, crushed them into a fine powder using a mortar and pestle, and pressed a holey carbon TEM grid onto the powder to adhere some to the grid. The LiH was prepared in an argon-filled glove box owing to its air sensitivity, and removed in a sealed vial which was opened under liquid N_2, eliminating air exposure. The other stable samples were also immediately placed under liquid N_2 after preparation to minimize unnecessary air exposure. On the F20, we used a probe current of about 75 pA. A total dose of less than 10^4 e^- Å^{-2} was applied to the oxides during acquisition, which we found was a few times lower than the dose necessary to induce a substantial change in the O K-edge fine structure. The LiH Li K-edge spectrum was acquired with a total dose of the order of 10^3 e^- Å^{-2}, and no change in fine structure was observed under any dose, measured to greater than 10^4 e^- Å^{-2}. All of the threshold damages for materials relevant to this study and the corresponding damage mechanisms are shown in Extended Data Table 2, and examples of damage series profiles used to establish these values are shown in Extended Data Fig. 6a.

To align the energy axis between the O K-edge spectra acquired on the Titan and the F20, we used the Li_2O peak at about 535 eV. The Li K-edge spectra were close enough to the zero-loss peak that no shifting of the spectra was necessary. In addition, spectra acquired on the F20 were bandpass-filtered by 0.6 eV to reduce noise below the energy resolution of the microscope. This reduced high-frequency noise while preserving larger features accurately, with only a slight reduction in sharp peaks. An example is shown for the Li_2O_2 O K-edge in Extended Data Fig. 3b.

Preparation of the coin-cell battery. Symmetric lithium cells (CR2032 coin cells) were assembled with two lithium electrodes (MTI Corp., 450 μm thick) and 1 M lithium hexafluorophosphate ($LiPF_6$) in ethylene carbonate:dimethyl carbonate (EC:DMC) (v:v = 1:1) as the electrolyte. Celgard 3501 was used as the separator. We subjected the cells to galvanostatic charging for 24 h at a current density of 1 mA cm^{-2}. A charging profile from one coin cell used is shown in Extended Data Fig. 7.

To plunge-freeze the samples, slush nitrogen was chosen to avoid detrimental interactions of the electrolyte with typical organic cryogens[37]. The slush was produced in the cryo-FIB workstation by vacuum-pumping liquid N_2 until it solidified. This enabled a higher cooling rate and reduced bubbling in the workstation. The coin cells were opened at the cryo-FIB workstation and the electrodes separated and immediately plunged into the slush nitrogen to preserve the electrolyte on the electrode. The frozen samples were then transferred into the preparation chamber attached to the cryo-FIB, typically sputter-coated with a 5–10-nm layer of metal (Pt or Au/Pd) to reduce charging, and transferred into the cryo-FIB chamber. Lift-out samples produced for cryo-STEM were transferred back to the workstation, where they were loaded into cryogenic sample storage boxes under liquid N_2 and transferred to a large liquid N_2 storage dewar. Cryo-TEM diffraction on lamellae produced by cryo-FIB lift-out showed that the electrolyte was frozen amorphously, and remained so throughout all of the preparation, transfer and characterization steps, as shown in Extended Data Fig. 8.

Three-dimensional reconstruction of cryo-FIB cross-sections. To reconstruct the three-dimensional dendrite structures, we used Avizo software (Thermo Fisher Scientific). Since the geometry of the FIB results in images of the cross-sections taken at oblique angles to the cross-section surface (the electron and ion columns are separated by 52° and the sample surface normal is positioned parallel to the ion beam for milling), the 30–50 individual images were aligned vertically by the position of the electrode surface and the appropriate length transformations were applied to the images to correct for the oblique viewing angle ($y = y'/\cos(\theta)$ and $z = z'/\sin(\theta)$, where y and z are the true depth and height of the object, respectively, y' and z' are the observed depth and height, and θ is the angle between the electrode surface normal and the electron beam). The dendrite and electrode structures were segmented by hand within each of the cross-sectional images, and these segmentations were connected in the perpendicular direction to reconstruct the three-dimensional structure.

EELS map processing. The large field of view of some EELS maps results in an energy shift of the entire spectrum at different points in the map. To accurately

map edges and analyse edge fine structure across the field of view, the energy axis at each pixel was shifted to the proper location. Each map was acquired in DualEELS mode, with both low-loss and high-loss regions of the spectrum recorded. The low-loss maps included the zero-loss peak, the position of which was used to align the energy axis of the low- and high-loss regions of the spectra simultaneously, resulting in a flat energy surface across the map.

To map elemental distributions, standard background subtractions were performed using a linear combination of power laws fit and local background averaging with a full-width at half-maximum of five pixels to increase the background signal-to-noise ratio[38]. Energy windows wider than the fine structure at the edge onset were integrated for elemental mapping, to minimize the effects of spatially varying fine structure on the apparent elemental concentrations. The fine structure of the edges was analysed by multivariate curve resolution (MCR), which solves for a specified number of linearly independent spectral components in the data by means of a local minimization. A non-negativity constraint was imposed on the corresponding concentration profiles, since negative concentrations are not physical, but the spectra were not constrained. To improve the signal-to-noise ratio for the MCR process, the data was typically binned by four (spatially) before analysis. To display the spatial distribution of the resulting spectral components, we fitted them back to the original data using Matlab's QR solver, which takes advantage of QR factorization to minimize the residual of the equation $SC = D$. In our case, S is the matrix of spectral components returned by MCR, C is the matrix of concentrations to be solved for and D is the matrix of original data. Using the original unbinned data (for the type I maps) or the original data binned by two (for the type II maps), we produced maps from the concentration matrix C for the corresponding MCR spectral components, such as in Fig. 3.

Data availability. The data that support the findings of this study are available from the corresponding author on reasonable request.

31. Tate, M. W. et al. High dynamic range pixel array detector for scanning transmission electron microscopy. *Microsc. Microanal.* **22**, 237–249 (2016).
32. Egerton, R. F., Li, P. & Malac, M. Radiation damage in the TEM and SEM. *Micron* **35**, 399–409 (2004).
33. Lin, F., Markus, I. M., Doeff, M. M. & Xin, H. L. Chemical and structural stability of lithium-ion battery electrode materials under electron beam. *Sci. Rep.* **4**, 5694 (2014).
34. Miki, T., Ikeya, M., Kondo, Y. & Kanzaki, H. Reflectance spectrum of lithium hydride at the Li K-absorption edge. *Solid State Commun.* **39**, 647–649 (1981).
35. Liu, D.-R. Electron energy loss spectroscopy of LiH with a scanning transmission electron microscope. *Solid State Commun.* **63**, 489–493 (1987).
36. Parades Mellone, O. A., Ceppli, S. A., Arneodo Larochette, P. P. & Stutz, G. E. Excitación de electrones K del Li a baja transferencia de momento por dispersión inelástica de rayos X en LiH. *Anal. Asoc. Fís. Argentina* **26**, 93–97 (2015).
37. Kesselman, E. et al. Cryogenic transmission electron microscopy imaging of vesicles formed by a polystyrene−polyisoprene diblock copolymer. *Macromolecules* **38**, 6779–6781 (2005).
38. Cueva, P., Hovden, R., Mundy, J. A., Xin, H. L. & Muller, D. A. Data processing for atomic resolution electron energy loss spectroscopy. *Microsc. Microanal.* **18**, 667–675 (2012).

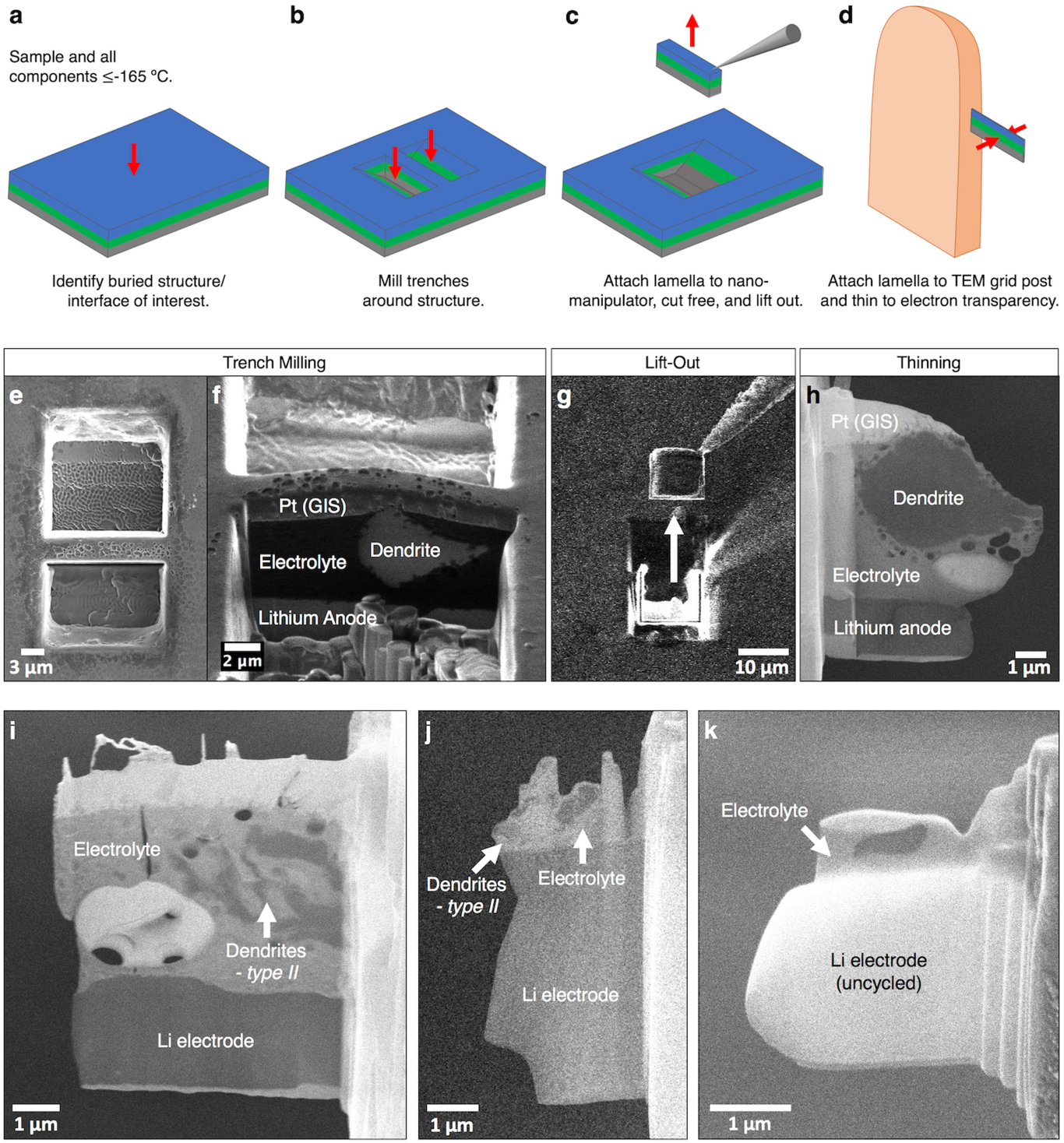

Extended Data Fig. 1 | Schematic and SEM images of the cryo-FIB lift-out sample preparation process, and examples of additional final lamellae. a, A buried structure or interface is identified for preparation, here a dendrite embedded in frozen electrolyte above the anode (indicated by the red arrow). In our coin-cell batteries, raised regions of electrolyte were used to localize buried dendrites. **b**, **e**, **f**, Trenches are then site-specifically milled around the site of interest, forming a vertical cross-sectional lamella containing the structure or interface. The sample is aligned in the microscope so that the electrode surface normal is parallel to the electron beam direction in **e**, and tilted by 52° to image the lithium anode–electrolyte interface and the electrolyte-embedded dendrite in **f**. **c**, **g**, A cooled nanomanipulator needle is then attached to the cryo-immobilized lamella by water vapour from a gas-injection system deposited as amorphous ice. The lamella is then cut free from the sample and lifted out. **d**, **h**, Finally, the lamella is attached to a TEM grid post with additional ice deposition, cut free from the nanomanipulator and thinned to electron transparency with the ion beam. **i**, **j**, Lamellae containing type II dendrites above lithium electrodes. The lamella in **i** contains a fluorine-rich structure as well. Different electrolyte thicknesses and milling parameters were used to prepare these lamellae, resulting in different final dimensions. **k**, A lamella produced from an uncycled electrode, used to obtain reference spectra. The increased signal of the uncycled electrode is due to different image-acquisition parameters, not a material difference.

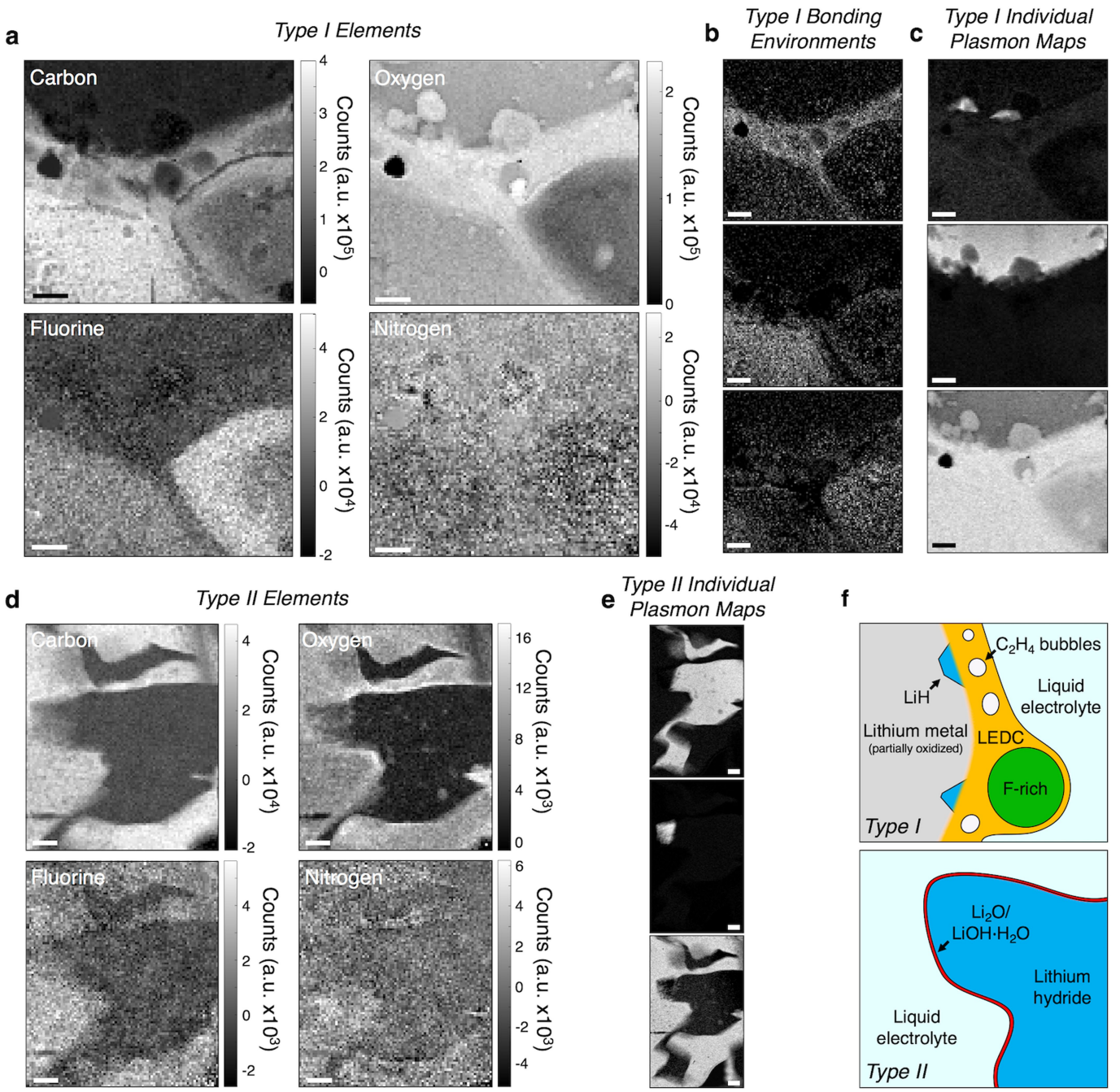

Extended Data Fig. 2 | Elemental maps of the regions near both types of dendrite surface, carbon-bonding environment maps resulting from fitting of MCR spectra back to original data, and corresponding summary schematics of both dendrite types and their SEI layers. Carbon, oxygen and fluorine are shown in a composite map in Fig. 2. **a**, **d**, Individual elemental maps showing the full count range, excluding 0.2% of high- and low-intensity outliers, make it clear that there is a substantial concentration of oxygen in the type I dendrite and very little in the type II dendrite, and that there is increased oxygen in the type I SEI compared to the electrolyte. In addition, essentially no fluorine is present in the type I SEI, and the large fluorine-rich structure contains a higher fluorine concentration than the electrolyte. Nitrogen maps are included as well, and largely show noise with little spatial dependence. Corresponding count scale bars are shown next to each map. **b**, Individual maps determined by MCR corresponding to the spectra primarily located at (and labelled in Fig. 3 as) the SEI, electrolyte and fluorine-rich structure (top to bottom), displaying the original counts. **c**, **e**, Individual plasmon maps determined by MCR for LiH, lithium and the electrolyte (top to bottom), displaying the original counts. **f**, Top, type I dendrites consist of partially oxidized lithium metal with small LiH regions at the surface, and have an extended SEI layer consistent with lithium ethylene dicarbonate (LEDC) that contains bubbles, probably from ethylene, a by-product of the SEI formation. Large fluorine-rich structures are often found near the dendrites. Bottom, type II dendrites consist of uniform LiH and have a compact $Li_2O/LiOH \cdot H_2O$ SEI layer. Although not depicted, fluorine-rich structures were also observed near type II dendrites. Scale bars, 300 nm.

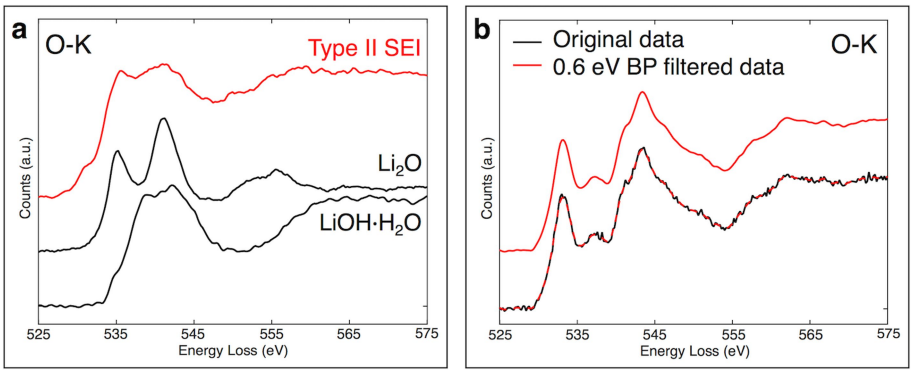

Extended Data Fig. 3 | Comparison of the type II SEI oxygen K-edge with reference spectra and an example of a bandpass-filtered spectrum. **a**, The O K-edge of the type II dendrite appears to be consistent with a combination of Li_2O and $LiOH \cdot H_2O$. Spectra are offset vertically for clarity. **b**, A 0.6-eV bandpass (BP) filter was applied to the O K-edge spectra acquired on the F20 to remove high-frequency noise. This preserved the main features of the edge while eliminating those below the energy resolution of the instrument.

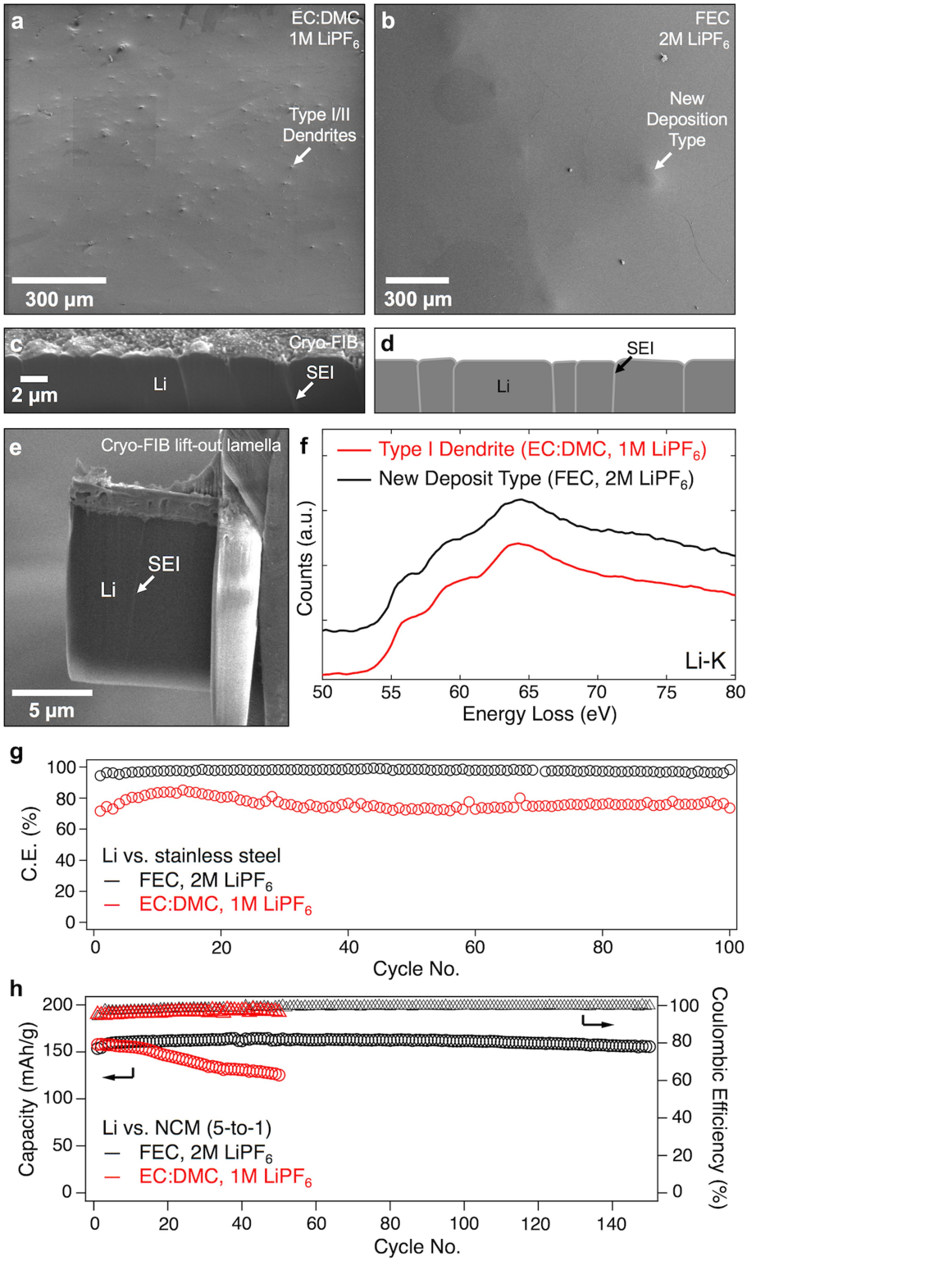

Extended Data Fig. 4 | Cryo-FIB, cryo-STEM EELS and electrochemical results comparing lithium deposition in cells using traditional and full-fluoride electrolytes. a, **b**, Cryo-FIB reveals that the dendrite density is much lower for the full-fluoride fluoroethylene carbonate (FEC) electrolyte (**b**) than with the traditional EC:DMC electrolyte (**a**). In the former case, nearly no LiH dendrites are present and the lithium deposition is modified, forming broad localized depositions. **c**, **d**, Cross-sections of these deposits reveal that they are composed of many smaller 'blocks' in contact, separated by SEI layers. **e**, **f**, A lamella of this type of deposition was prepared by cryo-FIB lift-out (**e**) and cryo-STEM EELS of the Li K-edge of the material revealed that it is composed of partially oxidized lithium metal (**f**), as was the type I dendrite in the traditional electrolyte. **g**, The Coulombic efficiency measured in a lithium versus stainless steel set-up using a constant current density of 1 mA cm^{-2} and capacity of 1 mAh cm^{-2} was greatly improved for the full-fluoride electrolyte compared to the traditional electrolyte. **h**, Cycling of a full cell comprising a lean lithium anode (50 µm) and a nickel manganese cobalt oxide (NCM) cathode (2 mAh cm^{-2}) with the full-fluoride electrolyte resulted in a substantial decrease in capacity fade and improved Coulombic efficiency over the traditional electrolyte. The discharge capacity is plotted on the left axis, whereas the Coulombic efficiency is on the right axis. The operating voltage range was 4.3 V to 3 V. In all figures, the red lines and symbols represent results for the EC:DMC, 1 M $LiPF_6$ electrolyte, whereas the black lines and symbols are for FEC, 2 M $LiPF_6$.

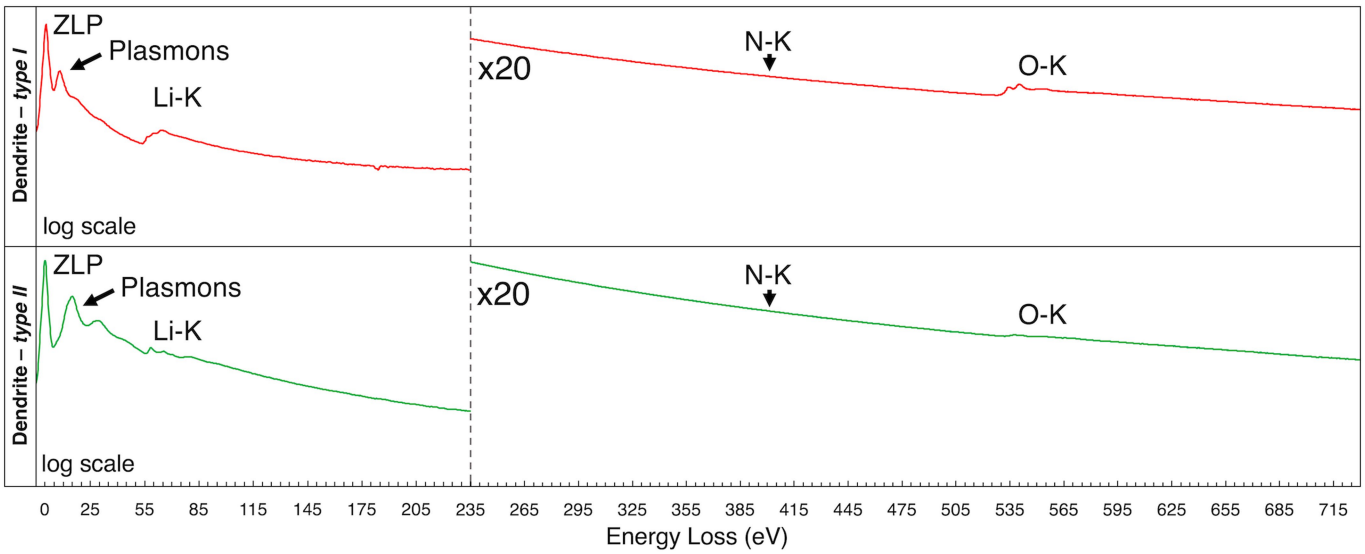

Extended Data Fig. 5 | Full spectra recorded from the dendrites (intensities on a logarithmic scale). The spectra show clear differences in the plasmons and Li K-edges, as well as a large difference in oxygen content between the type I and type II dendrites. The small amount of oxygen on the type II dendrite is probably due to water molecules adsorbed on the surface of the sample in the microscope vacuum, which would typically react with materials such as lithium or sodium at room temperature. No nitrogen was present in either dendrite, confirming that no reaction with nitrogen in the air or liquid N_2 had occurred.

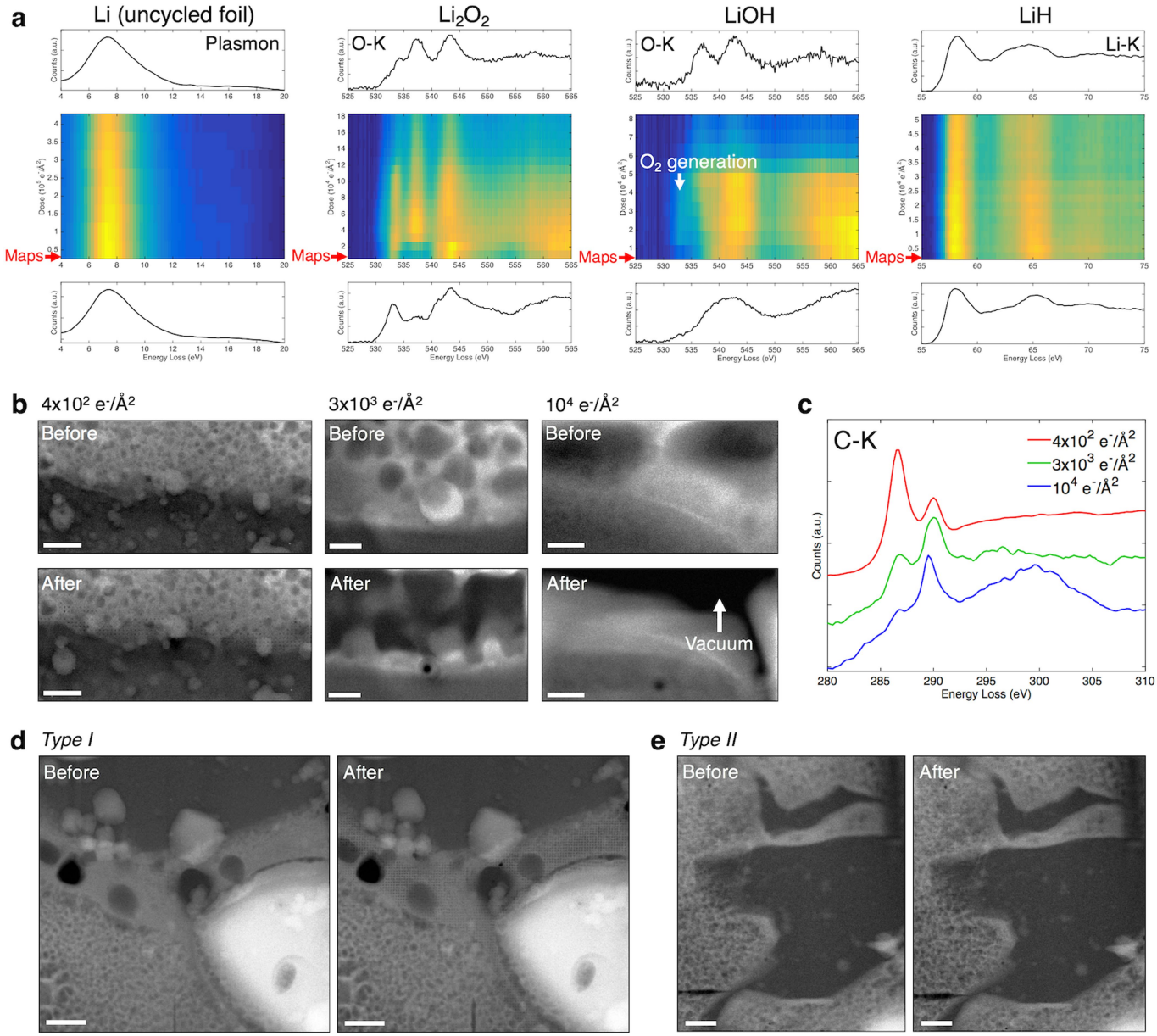

Extended Data Fig. 6 | Example damage series profiles and initial/final spectra taken for lithium materials relevant to this study over a range of doses at which damage occurs, dark-field cryo-STEM images of various types of damage induced in a frozen organic electrolyte at different doses with corresponding spectra, and before and after images of the regions in which the EELS maps in the main text were taken. All spectra were recorded at cryogenic temperatures. **a**, We found all oxide materials convert to Li_2O under large doses. Li_2O and LiH are primarily affected by mass loss, with no substantial changes in fine structure. The maps presented in the main text were acquired at doses lower than the dose indicated by the red arrows shown at the bottom of the plots, of the order of 10^2 e^- Å^{-2}. **b**, **c**, While some structural modification of the electrolyte material was present at low doses, probably due to liberation of hydrogen, a dose greater than 10^3 e^- Å^{-2} was required for substantial mass loss and modification of spectral fine structure. At 3×10^3 e^- Å^{-2}, approximately 50% of the material remained after the map, as determined by the ADF signal. At 10^4 e^- Å^{-2}, the material was completely removed in some areas, but the carbonate portion of the molecule remained. Doses applied during acquisition of the maps in the main text were less than the lowest dose shown here. Spectra are offset vertically for clarity. **d**, **e**, In the maps displayed in the main text, small structural changes were observed in the organic materials, which is expected given our damage analysis. This is probably due to liberation of hydrogen from the molecules, which occurs at low dose. The fine structure is not greatly affected until approximately an order of magnitude higher dose than was applied during these maps, which was of the order of 10^2 e^- Å^{-2}. Scale bars, 200 nm, 30 nm and 60 nm (**b**, left to right), 300 nm (**d**, **e**).

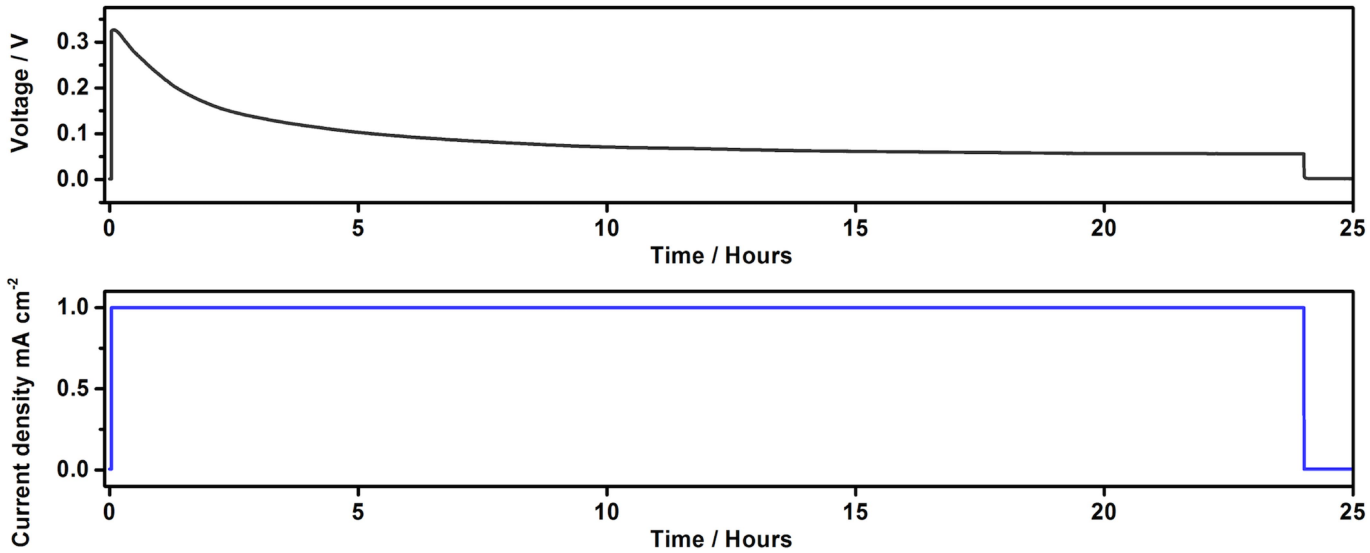

Extended Data Fig. 7 | Charging profile from a symmetric lithium coin cell. A constant current of 1 mA cm^{-2} was applied to the cells for 24 h (bottom). The resulting voltage profile from one of the coin cells used is shown in the top panel.

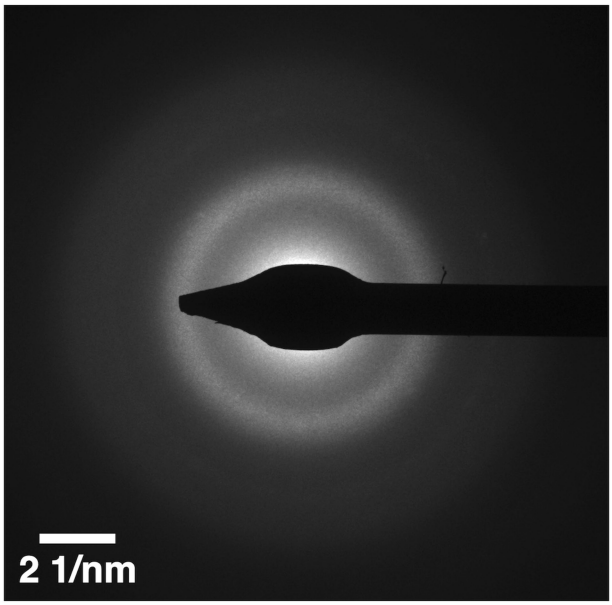

Extended Data Fig. 8 | Amorphous diffraction pattern of the electrolyte recorded in a cryo-lamella produced by cryo-FIB lift-out. Cryo-TEM diffraction of the electrolyte on samples produced by cryo-FIB lift-out shows that it is frozen amorphously and does not recrystallize at any point during the preparation, storage, transfer or characterization.

Extended Data Table 1 | Comparison of the properties of type I and II dendrites

Property	Dendrite Type I	Dendrite Type II
Diameter	~1-10 μm	~100s of nm
Morphology	Low curvature	Tortuous
Electrode Contact Area	~10 μm^3	~0.1 μm^3
Composition	Lithium metal, slightly oxidized (Li_2O).	LiH
Distribution of Materials	Slightly oxidized lithium with small LiH regions on surface.	Uniform LiH. Pure/slightly oxidized Li particle on tip.
SEI Thickness	~300-500 nm	~20 nm
SEI Elements Detected	Li, C, O	Li, O
SEI Composition	Extended SEI consistent with lithium ethylene dicarbonate. Large bubbles within likely originate from ethylene gas.	Li_2O and $LiOH{\cdot}H_2O$

Extended Data Table 2 | Threshold electron doses and primary damage mechanisms observed for relevant materials

Material	Damage Dose ($e^-/Å^2$)	Primary Damage Mechanism
Li (uncycled foil)	10^5	Mass loss/Minimal Li_2O formation
Li_2O	$>10^5$	Mass loss
Li_2O_2	$>10^4$	Mass loss/Li_2O conversion
LiOH	10^4	O_2 generation/Mass loss/Li_2O conversion
LiH	$>10^4$	Mass loss
EC:DMC - 1M $LiPF_6$	$<10^2$ $>10^3$ 10^4	Slight structural modifications Mass loss/Initial fine structure changes Large mass loss/Conversion to Li_2CO_3

All of the damage thresholds listed are for cryogenic samples under a 300-kV electron beam. The primary damage mechanism of lithium is mass loss. While a very small amount of oxide can form, this is much less than the initial oxide impurities in an uncycled electrode, and occurs at more than 10^5 e^- $Å^{-2}$. Li_2O_2 and LiOH both initially suffer mass loss at or above 10^4 e^- $Å^{-2}$ and subsequently begin converting to Li_2O at higher doses, whereas Li_2O suffers only mass loss and no change in fine structure. LiH is stable to above 10^4 e^- $Å^{-2}$, with mass loss occurring above this and little to no oxidation. The electrolyte material damages differently at different doses, with slight structural modifications occurring at low doses and mass loss and changes in fine structure occurring above 10^3 e^- $Å^{-2}$. At 10^4 e^- $Å^{-2}$, a substantial portion of the mass is lost, leaving behind the carbonate portion of the solvent molecules, the fine structure of which is still intact at this dose.